

Structure of a Specialized Acyl Carrier Protein Essential for Lipid A Biosynthesis with Very Long-Chain Fatty Acids in Open and Closed Conformations

Theresa A. Ramelot,^{*,†} Paolo Rossi,[‡] Farhad Forouhar,[§] Hsiao-Wei Lee,^{||} Yunhuang Yang,[†] Shuisong Ni,[†] Sarah Unser,[†] Scott Lew,[§] Jayaraman Seetharaman,[§] Rong Xiao,[‡] Thomas B. Acton,[‡] John K. Everett,[‡] James H. Prestegard,^{||} John F. Hunt,[§] Gaetano T. Montelione,^{‡,⊥} and Michael A. Kennedy^{*,†}

[†]Department of Chemistry and Biochemistry, Northeast Structural Genomics Consortium, Miami University, Oxford, Ohio 45056, United States

[‡]Center for Advanced Biotechnology and Medicine, Department of Molecular Biology and Biochemistry, and Northeast Structural Genomics Consortium, Rutgers, The State University of New Jersey, Piscataway, New Jersey 08854, United States

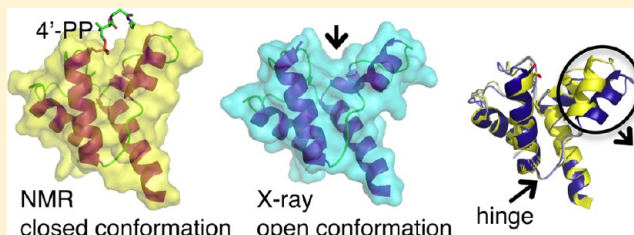
[§]Department of Biological Sciences, Northeast Structural Genomics Consortium, Columbia University, New York, New York 10027, United States

^{||}Complex Carbohydrate Research Center, Northeast Structural Genomics Consortium, University of Georgia, Athens, Georgia 30602, United States

[⊥]Department of Biochemistry, Robert Wood Johnson Medical School, University of Medicine and Dentistry of New Jersey, Piscataway, New Jersey 08854, United States

S Supporting Information

ABSTRACT: The solution nuclear magnetic resonance (NMR) structures and backbone ¹⁵N dynamics of the specialized acyl carrier protein (ACP), RpAcpXL, from *Rhodopseudomonas palustris*, in both the apo form and holo form modified by covalent attachment of 4'-phosphopantetheine at S37, are virtually identical, monomeric, and correspond to the closed conformation. The structures have an extra α -helix compared to the archetypical ACP from *Escherichia coli*, which has four helices, resulting in a larger opening to the hydrophobic cavity. Chemical shift differences between apo- and holo-RpAcpXL indicated some differences in the hinge region between $\alpha 2$ and $\alpha 3$ and in the hydrophobic cavity environment, but corresponding changes in nuclear Overhauser effect cross-peak patterns were not detected. In contrast to the NMR structures, apo-RpAcpXL was observed in an open conformation in crystals that diffracted to 2.0 Å resolution, which resulted from movement of $\alpha 3$. On the basis of the crystal structure, the predicted biological assembly is a homodimer. Although the possible biological significance of dimerization is unknown, there is potential that the resulting large shared hydrophobic cavity could accommodate the very long-chain fatty acid (28–30 carbons) that this specialized ACP is known to synthesize and transfer to lipid A. These structures are the first representatives of the AcpXL family and the first to indicate that dimerization may be important for the function of these specialized ACPs.



The specialized acyl carrier proteins (ACPs) known as AcpXLs are small acidic proteins that are involved in the biosynthesis of lipid A, by incorporation of a very long-chain fatty acid (VLCFA), typically with 28–30 carbons. The designation AcpXL was first given to the specialized *Rhizobium leguminosarum* ACP that has an attached VLCFA, 27-hydroxyoctacosanoic acid (27-OH-C₂₈).¹ AcpXL proteins are conserved among bacteria from the order Rhizobiales, including species from the genera *Rhodopseudomonas*, *Rhizobium*, *Sinorhizobium*, *Brucella*, and *Bartonella*. The *acpXL* gene is typically found in a six-gene cluster that is responsible for the synthesis of VLCFA-modified lipid A.^{2–4} Lipid A is the membrane-located component of lipopolysaccharide (LPS), the

major surface component of Gram-negative bacteria. VLCFA-modified LPS has been identified in many species of nitrogen-fixing bacteria, as well as some intracellular pathogens, like *Brucella* and *Bartonella* species, which can form chronic intracellular infections.⁵

AcpXL is essential for the biosynthesis of VLCFA-modified lipid A in both the free-living and symbiotic states in the well-studied *Rhizobiales* species, *Sinorhizobium meliloti*, and *R. leguminosarum*.^{3,4,6–9} Although it is not indispensable for their

Received: April 27, 2012

Revised: August 8, 2012

Published: August 9, 2012



growth or colonization of legumes, the absence of VLCFA-LPS resulted in increased sensitivity to environmental stresses, such as changes in salt, detergents, or increased acidity, and abnormal bacteroid development or reduced competitiveness for legume symbiosis.^{3,4,6–9} It has also been hypothesized that VLCFA-LPS is needed for infection of medically important pathogens like *Brucella* species that are incorporated into membrane-bound acidic compartments in the mammalian host (reviewed in ref 10). With mutations in the *acpXL* gene, neither *S. meliloti* or *R. leguminosarum* can produce VLCFAs.^{4,6,7,11}

In the well-studied synthesis of lipid A in *Escherichia coli*, the ACP shuttles the growing fatty acid chain between component enzymes during chain elongation and modification. To allow this, the active form, holo-ACP, has a long 4'-phosphopantetheine (4'-PP) arm of ~18 Å that carries the growing acyl intermediates as thioesters attached to the terminal thiol of the 4'-PP. Conversion to holo-ACP is conducted by holo-ACP synthase (AcpS), which covalently attaches a 4'-PP moiety of coenzyme A to the hydroxyl group of a serine residue located within a highly conserved DSL sequence via a phosphodiester bond. Movement of the flexible 4'-PP alternately shelters the intermediate within the hydrophobic core of the ACP or exposes it to enzymes for further modification. In the "prototypical" lipid A synthesis, 3-hydroxymyristoyl-(3-OH-C₁₄)-ACP is involved in the first two primary acylation reactions, and lauroyl- and myristoyl-ACPs provide the FA for secondary acylation reactions. However, for the synthesis of the specialized VLCFA lipid, a long OH-FA, such as the saturated 27-OH-C₂₈ or 29-OH-C₃₀, is typically incorporated at the secondary or "piggyback" position, resulting in a pentacylated lipid A.

Here we report the solution structure of the small (10.2 kDa), acidic (pI 4.4) AcpXL from *Rhodospseudomonas palustris*, RpAcpXL (gene *rpa2022*, GenBank entry NP_947367.1, UniProtKB entry Q6N882, KEGG entry *rpa*:RPA2022, NESG entry RpR324), in both the apo and 4'-PP-modified forms. *R. palustris* are Gram-negative purple non-sulfur bacteria that can switch among four different modes of metabolism. Notably, *R. palustris* can fix nitrogen, like many other rhizobia, although it is not in the same Rhizobiaceae family as *S. meliloti* and *R. leguminosarum* but rather belongs to the Bradyrhizobiaceae family. Because the sequence of RpAcpXL is >70% identical with those found in other Rhizobiales bacteria (more than 60 sequences found in a blast search of KEGG orthologs), it is a structural representative for this family of proteins. High-resolution structures of both apo- and holo-RpAcpXL were determined by solution NMR spectroscopy, and the apo-RpAcpXL structure was also determined by X-ray crystallography at 2.0 Å resolution. Given that ACPs must interact with dozens of proteins to synthesize and transfer acyl chains to lipid A,¹² competition and regulation may be important. Because it has been suggested that structural adjustments of the ACP resulting from phosphopantetheinylation and subsequent acylation might result in allosteric regulation of interactions with other enzymes, we have examined the structure and backbone ¹⁵N dynamics of RpAcpXL both with and without the 4'-PP modification. This is a first step toward understanding the structure and function of proteins in the AcpXL family.

■ EXPERIMENTAL PROCEDURES

Expression, Purification, and Characterization of >90% Apo-RpAcpXL. The *RpAcpXL* gene was cloned into

a pET21-based expression vector (NESG clone entry RpR324-21.4), which has been deposited in the PSI:Biological Materials Repository¹³ (<http://psimr.asu.edu/>) as clone entry RpCD00339419. The RpAcpXL protein, which included a C-terminal His₆ tag (LEHHHHHH), was expressed and purified following standard protocols of the Northeast Structural Genomics Consortium (NESG) to prepare U-¹³C,¹⁵N and U-¹⁵N, 5% biosynthetically directed ¹³C (NC5) samples;¹⁴ see the Supporting Information for a detailed description of the sample preparation, NMR data acquisition, and structure determination methods. Se-Met-RpAcpXL for crystallization trials was primarily monomer based on analytical static light scattering in-line with gel filtration chromatography (GF/LS). NMR samples were purified from the monomer fraction during gel filtration chromatography and were characterized as monomeric under the conditions used in the NMR experiments [1.0 mM protein, 10% (v/v) D₂O, 20 mM MES, 200 mM NaCl, 10 mM DTT, and 5 mM CaCl₂ (pH 6.5) at 25 °C] based on correlation time estimates from one-dimensional ¹⁵N T₁ and T₂ relaxation data [estimated τ_c of 8 ns (Figure S1 of the Supporting Information)]. The level of biosynthetic incorporation of 4'-PP was determined to be <10% by mass spectrometry. Interestingly, the N-terminal methionine was ~50% cleaved in both the NC5 and [U-¹³C,¹⁵N]RpAcpXL samples.

Overexpression and Purification of *E. coli* AcpS. The p15Rv-L expression vector containing the gene encoding AcpS from *E. coli* K12 was transformed and expressed as previously described;¹⁵ however, a modified purification procedure is reported here. Soluble AcpS was obtained by denaturation of the pellet in 6 M urea, followed by refolding, rather than the previous method of purification from the soluble fraction after lysis and centrifugation.¹⁵ Pelleted cells were resuspended in 25 mL of lysis buffer [50 mM Tris, 10 mM MgCl₂, and 5% glycerol (pH 8.0)] and lysed by three passes through a French pressure cell (SLM Instruments). The resulting lysate was spun at 24000g for 60 min. The insoluble pellet was resuspended in 25 mL of lysis buffer containing 6 M urea by being stirred overnight at room temperature. After centrifugation at 12000g for 5 min, the soluble portion was loaded onto a 10 mL Ni-NTA affinity column (Qiagen) and washed with 50 mL of lysis buffer containing 30 mM imidazole and 6 M urea. The His₆-tagged AcpS was eluted from the column with lysis buffer containing 300 mM imidazole and 6 M urea. The purified protein (~10 mL) was diluted to 1.5 M urea by a 4-fold dilution with buffer and centrifuged at 12000g for 5 min to remove precipitation. Concentration of this protein by centrifugation resulted in a final protein concentration of ~400 µg/mL.

Enzymatic Conversion of <10% Holo-RpAcpXL to >95% Holo-RpAcpXL. To prepare samples of >95% [U-¹³C,¹⁵N]-holo-RpAcpXL and NC5 holo-RpAcpXL, the <10% holo-RpAcpXL was incubated with *E. coli* AcpS for coenzyme A (CoA)- and Mg²⁺-dependent conversion. The reaction mixtures contained 10 mM MgCl₂, 200 mM NaCl, 5% glycerol, 300 µM CoA, 100 µM RpAcpXL, 6.0 µM AcpS, 300 mM urea, and 30 mM Tris (pH 8.0) in a total volume of 10 mL. Reaction mixtures were incubated overnight at room temperature, and conversion to holo-RpAcpXL was confirmed by mass spectrometry [Bruker Autoflex III MALDI-TOF (Figure S2 of the Supporting Information)]. Samples were then buffer-exchanged to NMR buffer and concentrated by centrifugation to 1 mM holo-RpAcpXL. The >95%

Table 1. Summary of NMR Structural Statistics for Apo- and Holo-RpAcpXL Ensembles^a

	apo	holo
completeness of resonance assignments ^b (%)		
backbone	98.9	98.3
side chain	99.2	99.2
stereospecific methyl	100	100
conformationally restricting constraints ^c		
NOE constraints		
total	1621	1735
intraresidue ($i = j$)	328	344
sequential ($ i - j = 1$)	404	433
medium-range ($1 < i - j < 5$)	481	515
long-range ($ i - j \geq 5$)	408	443
no. of NOE constraints per residue	17.4	18.5
constraints for 4'-PP (intra/inter)	—	4/6
dihedral angle constraints	144	144
hydrogen bond constraints	94	94
NH RDC constraints (PEG/phage)	58/73	57/70
no. of constraints per residue (total)	20.0	21.0
no. of constraints per residue (long)	4.5	4.8
residual constraint violations ^c		
average no. of distance violations per structure		
0.1–0.2 Å	5.3	5.5
0.2–0.5 Å	0.6	1.4
>0.5 Å	0	0
maximal distance violation (Å)	0.4	0.4
ave rmsd for dihedral angle violations per structure		
>1–10°	1.2	1.4
>10°	0	0
ave rmsd violations per restraint		
distance (Å)	0.01	0.01
dihedral angle (deg)	0.2	0.3
maximal dihedral angle violation (deg)	5.0	5.3
RDC Q_{rmsd} (PEG/phage) ^d	0.1/0.2	0.2/0.3
model quality ^c		
rmsd from average coordinates (Å)		
backbone atoms (N, C ^α , C')	0.4	0.5
heavy atoms	0.8	0.9
rmsd for bond lengths (Å)	0.02	0.02
rmsd for bond angles (deg)	1.2	1.2
MolProbity Ramachandran summary ^e (%)		
most favored regions	98.4	98.1
allowed regions	1.4	1.9
disallowed regions	0.2	0.1
global quality scores (raw/Z score)		
Procheck G factor (ϕ, ψ) ^e	0.2/1.2	0.2/1.0
Procheck G factor (all dihedrals) ^e	0.1/0.7	0.1/0.7
Verify3D	0.4/−0.8	0.4/−1.0
ProsaII	0.9/1.0	0.9/0.9
MolProbity clashscore	14.2/−0.9	13.1/−0.7
RPF scores ^f		
recall/precision	99/92	99/92
F measure/DP score	95/85	95/86

^aStructural statistics were computed for the ensembles of 20 deposited structures (PDB entries 2LPK and 2LL8). ^bComputed for residues 1–93, using AVS software from the expected number of peaks.⁵⁰ ^cCalculated using PSVS version 1.4.⁵¹ Average distance constraints were calculated using the sum of r^{-6} values. ^dRDC goodness-of-fit quality factor Q_{rmsd} determined using PALES.⁵² ^eOrdered residue ranges [$S(\phi) + S(\psi) > 1.8$]: 4–92. ^fRPF scores⁵³ reflecting the goodness of fit of the final ensemble of structures (residues 1–101) to the NOESY data and resonance assignments.

[U-¹³C,¹⁵N]-holo-RpAcpXL contained ~10% ¹³C- and ¹⁵N-labeled 4'-PP and ~85–90% unlabeled 4'-PP because isotopic enrichment was dependent on the amount of ¹³C and ¹⁵N incorporated during expression and modification during

biosynthesis within *E. coli*. Further incorporation of the ~85–90% unlabeled 4'-PP was added by in vitro enzymatic conversion by AcpS using unlabeled CoA.

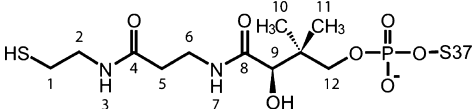
NMR Spectroscopy and Determination of the Structures of Apo- and Holo-RpAcpXL. NMR data for apo-RpAcpXL were collected at 25 °C on U-¹³C,¹⁵N and NCS samples of ~30 μL in 1.7 mm microprobe NMR tubes on a Bruker Avance 600 MHz spectrometer equipped with a 1.7 mm TCI Micro CryoProbe. Collection of NMR data, chemical shift assignments, and structure calculations were conducted as previously described¹⁶ and as described briefly in the Supporting Information. The final coordinates for the ensemble of 20 structures and NMR-derived constraints for apo-RpAcpXL were deposited in the Protein Data Bank (PDB) as entry 2KW2, and chemical shifts and NOESY peak lists were deposited in BioMagResBank (entry 16805).

Additional NMR data for apo-RpAcpXL and data for holo-RpAcpXL were collected at 25 °C on U-¹³C,¹⁵N and NCS samples of ~250 μL in 5 mm Shigemi NMR tubes on 600 MHz Varian Inova and 850 MHz Bruker Avance III NMR spectrometers. D₂O-exchanged samples were prepared by freezing U-¹³C,¹⁵N samples followed by overnight lyophilization and resuspension in 99.9% D₂O (Acros Organics). Assignments of holo-RpAcpXL ¹H, ¹³C, and ¹⁵N resonances were based on assignments for apo-RpAcpXL and confirmed by analysis of conventional triple-resonance spectra, including three three-dimensional (3D) NOESY experiments ($\tau_m = 70$ ms). The NOESY spectra were collected on both apo- and holo-RpAcpXL with identical parameters and the same NMR instrument (850 MHz Bruker Avance III NMR) to facilitate the comparison. Additional NOEs for holo-RpAcpXL were assigned from a four-dimensional ¹³C-¹³C HMQC-NOESY-HMQC experiment ($\tau_m = 70$ ms) in a D₂O solution. Amide backbone one-bond ¹H-¹⁵N residual dipolar coupling (RDC) values of apo- and holo-RpAcpXL were measured by comparing data for isotropic and two partially aligned NCS samples in Pf1 phage (12.5 mg/mL) and polyethylene glycol bicelles (4.2%) as previously described.^{17–19} Spectra were processed with NMRPipe²⁰ and analyzed with Sparky 3.110 (T. D. Goddard and D. G. Kneller). Chemical shifts observed in an overlay of the ¹H-¹⁵N HSQC spectra of apo-RpAcpXL versus holo-RpAcpXL (Figure S3 of the Supporting Information) indicated amide cross-peaks that were shifted by >0.05 ppm in the ¹H dimension. Chemical shift peak doubling was observed for residues S3 and T4 as a result of the incomplete processing of the N-terminal methionine after expression in *E. coli*.

The solution NMR structures of apo- and holo-RpAcpXL were calculated using NOESY data collected under identical conditions and parameters and refined with an identical protocol, with the exclusion of 4'-PP in the apo-RpAcpXL structure calculation. Initial structures were calculated with CYANA 3.0²¹ using resonance assignments, NOESY peak lists from three or four NOESY spectra, dihedral restraints derived from TALOS+,²² and two sets of ¹H-¹⁵N RDCs. Chemical shifts for the 4'-PP prosthetic group were assigned manually. CYANA structures were refined with CNS in explicit water^{23,24} using molecular parameter and topology files created for the 4'-PP prosthetic group with fmcGui.²⁵ Structural statistics for apo- and holo-RpAcpXL are listed in Table 1. The final coordinates for the ensemble of 20 structures and NMR-derived constraints for both apo- and holo-RpAcpXL were deposited in the Protein Data Bank as entries 2LPK and 2LL8, respectively, and chemical shifts and NOESY FIDs and peak lists were deposited in the BioMagResBank as entries 18263 and 18032, respectively. The 4'-PP chemical shifts were deposited in the

BioMagResBank along with holo-RpAcpXL shifts and are listed in Table 2.

Table 2. Chemical Shifts of NMR Assignable Atoms in 4'-Phosphopantetheine (4'-PP) in Holo-RpAcpXL



position	atom	proton	¹³ C/ ¹⁵ N [¹ H] (ppm)
1	C43	H43*	26.2 (2.54, 2.54)
2	C42	H42*	45.2 (3.29, 3.29)
3	N41	H41	123.7 (8.15)
4	C39		176.3
5	C38	H38*	38.2 (2.49, 2.49)
6	C37	H37*	38.2 (3.51, 3.51)
7	N36	H36	119.6 (8.02)
8	C34		177.3
9	C32	H32	77.1 (4.00)
10	C31	H31*	26.0 (0.95)
11	C30	H30*	26.0 (0.95)
12	C28	H28*	73.8 (3.45, 3.74)

Backbone ¹⁵N dynamics data were collected on apo- and holo-RpAcpXL samples at a ¹⁵N Larmor frequency of 60.8 MHz at 25 °C on a Bruker Avance III 600 MHz spectrometer running Topspin 3.0. Residue specific ¹⁵N longitudinal and transverse times (T_1 and T_2 , respectively) and ¹⁵N{¹H} heteronuclear NOE values were calculated from cross-peak intensities in the respective two-dimensional (2D) experiments. T_1 and T_2 experiments were conducted as pseudo-3D experiments. T_1 spectra were acquired with relaxation delays of 0.05, 0.1, 0.2, 0.3, 0.4, 0.6, 0.8, 1.0, 1.2, 1.5, and 2.0 s and a recycle delay of 3 s. T_2 spectra were acquired with CPMG delays of 16, 32, 48, 64, 80, 96, 128, 160, 192, 240, 304, and 384 ms and a recycle delay of 1.5 s. Data for overlapped resonances was omitted from all analyses. T_1 and T_2 were computed by Protein Dynamics Center (Bruker version 1.2.3) by fitting peak intensity as a function of delay times according to standard equations for exponential decay. Error bars were estimated by the Protein Dynamics Center based on the fit to the data. T_1 and T_2 values are plotted versus residue in Figure 2. The ¹⁵N{¹H} heteronuclear NOE was collected as two 2D interleaved spectra with and without a default proton saturation delay of 3 s and a recycle delay of 5 s. ¹⁵N{¹H} heteronuclear NOE values were determined from the ratio of the peak intensities obtained after processing with NMRPipe,²⁰ peak picking in Sparky, and using Microsoft Excel to obtain and plot the ratio versus the residue (Figure 2).

Crystallization and Determination of the X-ray Structure of Apo-RpAcpXL. Crystals of Se-Met labeled apo-RpAcpXL were grown using the microbatch method at 4 °C; 2 μL of protein solution in buffer containing 100 mM NaCl, 5 mM DTT, 0.02% NaN₃, and 10 mM Tris-HCl (pH 7.5) was mixed with 2 μL of crystallization cocktail composed of 0.1 M sodium citrate (pH 4.2), 12% PEG 20K, and 0.1 M lithium sulfate. Crystals appeared after a few days and were subsequently flash-frozen using the crystallization cocktail described above that contained 15% glycerol as a cryoprotectant. A 2.0 Å resolution single-wavelength anomalous diffraction (SAD) data set was collected at the peak absorption wavelength of selenium at beamline X4C of the National

Synchrotron Light Source. The diffraction images were processed with the HKL package.²⁶ Initial attempts to determine the structure by the SAD method were unsuccessful as the initiating Se-Met, which was the only Se-Met in the protein, was disordered. Subsequently, the structure was determined by molecular replacement using Molrep.²⁷ The solution state NMR structure of apo-RpAcpXL was initially used as the search model for structure determination (residues 3–91 with hydrogen atoms removed), which gave a solution with R_{work} and R_{free} values of 45.8 and 53.3, respectively, after refinement using CNS.²³ However, inspection of the electron density map revealed that residues 57–73 comprising $\alpha 3$ and the loop that connects it to $\alpha 4$ had very poor electron density. After the biased region (residues 57–73) had been removed from the structure, a second round of refinement was performed, which significantly improved the map and R_{work} and R_{free} values to 39.1 and 43.3, respectively. Consequently, model building was performed using XtalView²⁸ and refined with CNS. Data collection and refinement quality statistics are summarized in Table 3, and the structure and structure factors are deposited in the PDB as entry 3LMO. Attempts to crystallize holo-RpAcpXL under the same conditions were unsuccessful.

RESULTS

Apo- and Holo-RpAcpXL NMR Structures. The solution NMR structures of apo- and holo-RpAcpXL (PDB entries 2LPK and 2LL8, respectively) were essentially the same (Figure 1A,B). The average pairwise backbone and heavy atom rmsd's between the apo and holo structures were 0.6 ± 0.1 and 1.0 ± 0.1 Å, respectively. Structure and quality statistics are listed in Table 1. There are five helices, with four of them ($\alpha 1$ – $\alpha 3$ and $\alpha 5$) forming a right-twisted four-helix bundle with an up–down–up–down topology. The shortest helix ($\alpha 4$) is perpendicular to $\alpha 3$ and $\alpha 5$ and is across from S37 at the N-terminus of $\alpha 2$. Table 2 shows a schematic view of 4'-PP and its linkage to the O γ side-chain atom of S37, which is located in a conserved DSL motif. S37 is located at the entrance to a hydrophobic cavity that extends down the central core of the protein and is surrounded by all five helices. The solvent-accessible volume of the hydrophobic pocket was ~ 70 Å³, calculated using CASTp.²⁴ There is a large, 21-residue loop between $\alpha 1$ and $\alpha 2$ prior to S37 that is well-defined in the NMR ensemble and stabilized by hydrophobic residues that interact with the protein core (I18, I23, and I30) and by backbone hydrogen bonds (Figure 1C). Loop 2, between $\alpha 2$ and $\alpha 3$, is stabilized by a hydrogen bond between L55 H^N and the side-chain COO[−] group of D48 in $\alpha 2$ (Figure 1C). This hydrogen bond is observed in most ACP structures and is believed to act as a hinge to allow for expansion of the cavity via an outward movement of $\alpha 3$. In holo-RpAcpXL, the only NOEs observed between the 4'-PP and the protein were to residues S37 and L38 (six NOEs). In addition, 4'-PP resonances were strong with narrow line widths indicating a dynamic structure. The 4'-PP chemical shifts were also typical of those expected for unstructured 4'-PP (Table 2). This is similar to results previously reported for other ACPs.^{30–32}

The structure of RpAcpXL differs from other previously determined ACP structures because it has an extra helix, $\alpha 4$, in the position following $\alpha 3$, making a total of five helices, whereas in the *E. coli* ACP, and most other ACPs, the structure consists of a four-helix bundle. Structural alignment of holo-RpAcpXL and *E. coli* ACP is shown in Figure 1D. The resulting effect is

Table 3. X-ray Data Collection and Refinement Statistics for Apo-RpAcpXL (PDB entry 3LMO)

	Se-Met
crystal parameters	
space group	P3 ₂ 21
unit cell dimensions	
<i>a</i> , <i>b</i> , <i>c</i> (Å)	62.73, 62.73, 60.12
α , β , γ (deg)	90, 90, 120
Matthews coefficient (Å ³ /Da)	3.0
data quality	
X-ray wavelength (Å)	0.97852
resolution range (Å)	30–2.0 (2.07–2.00)
R_{merge} (%) ^a	3.3 (8.6)
no. of observations	109780
no. of reflections	16061
no. of reflections in the R_{free} set	784
mean redundancy	6.9 (4.8)
completeness (%)	89.9 (67.1)
mean I/σ_I	51.2 (14.6)
refinement residuals ($I \geq 2\sigma_I$)	
R_{free} (%) ^b	25.4 (25.7)
R_{work} (%) ^b	21.6 (21.1)
model quality ^c	
rmsd for bond lengths (Å)	0.006
rmsd for bond angles (deg)	1.0
MolProbity Ramachandran summary (%)	
most favored regions	100.0
allowed regions	0.0
disallowed regions	0.0
global quality score (raw/Z score)	
Procheck <i>G</i> factor (ϕ , ψ)	0.3/1.5
Procheck <i>G</i> factor (all dihedrals)	0.3/1.7
Verify3D	0.5/−0.2
ProsaII	1.0/1.5
MolProbity clashscore	3.5/0.9
model contents (no.)	
protomers in the asymmetric unit	1
protein residues	2–95
atoms in protein	728
water molecules	192
<i>B</i> factor (Å ²)	
protein	31.4
water molecules	35.0

^a $R_{\text{merge}} = \sum_{hkl} \sum_i |I_i(hkl) - \langle I(hkl) \rangle| / \sum_{hkl} \sum_i I_i(hkl)$, where $I(hkl)$ is the intensity of reflection hkl , \sum_{hkl} is the sum over all reflections, and \sum_i is the sum over *i* measurements of reflection hkl . ^b $R_{\text{free}} = \sum_{hkl} |F_{\text{obs}} - F_{\text{calc}}| / \sum_{hkl} F_{\text{obs}}$; R_{free} is calculated for a randomly chosen set (5%) of reflections that were not used for structure refinement, and R_{work} is calculated for the remaining reflections. ^cCalculated using PSVS version 1.4.⁵¹

that the hydrophobic cavity in RpAcpXL is slightly deeper because the lip on the cup ($\alpha 3$ and $\alpha 4$) extends higher.

For the *E. coli* ACP, cation binding stabilized the structure and stimulated FA synthesis.³³ Binding to divalent cations, such as Ca²⁺, Mg²⁺, and Mn²⁺, resulted in stabilization of the structure.^{33,34} Two Mn²⁺-binding sites were characterized by paramagnetic relaxation perturbation measurements: near the modified S36 and near the hinge region carboxylate, E47 (*E. coli* numbering).³⁵ In apo-RpAcpXL, small HN chemical shift changes were observed for L33, D36, S37, D39, D48, F51, and I53 in ¹H–¹⁵N HSQC spectra upon removal of Ca²⁺ and titration with Mg²⁺ (Figure S3A of the Supporting

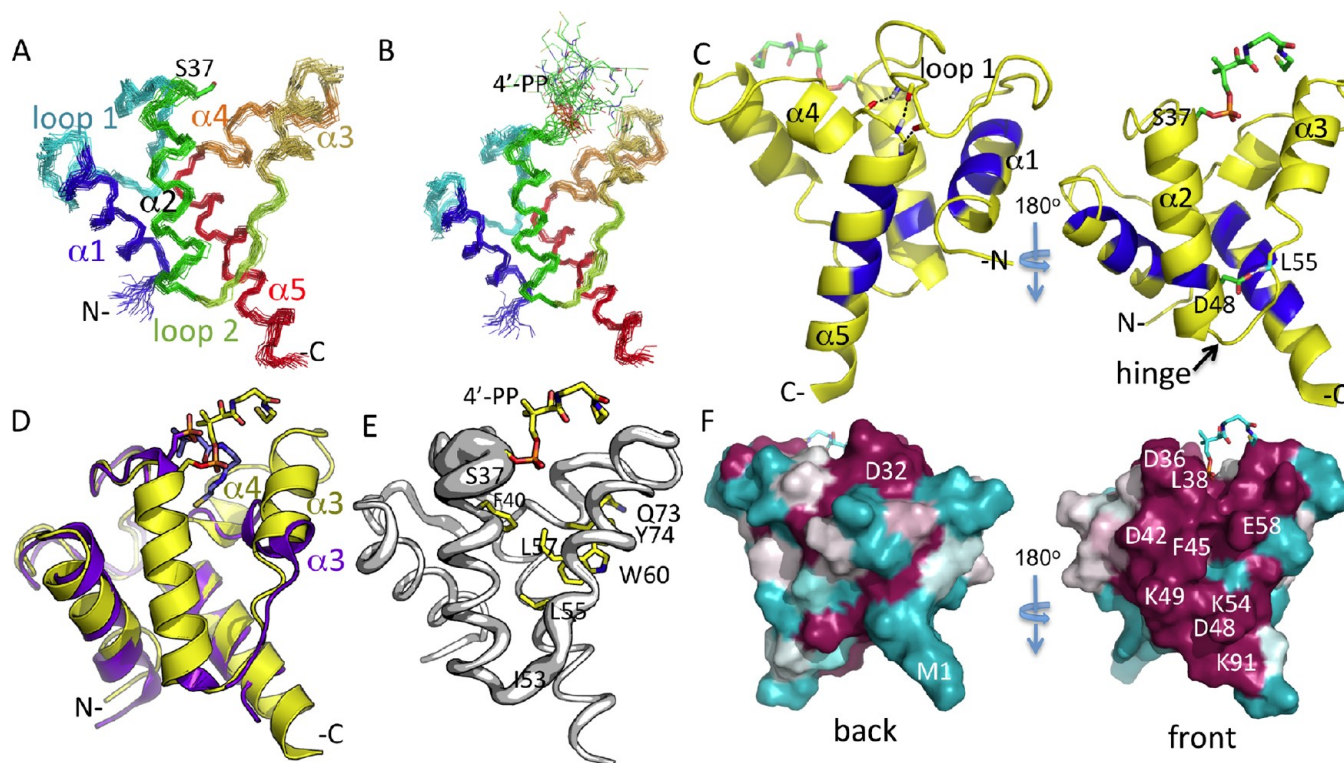


Figure 1. Backbone diagrams of the solution NMR structure of (A) apo-RpAcpXL (residues 2–93, PDB entry 2LPK) and (B) holo-RpAcpXL (residues 2–93, PDB entry 2LL8) with one selected 4'-PP indicated. (C) The left panels is a back cartoon view of a representative holo-RpAcpXL structure. Hydrogen bonds stabilizing loop 1 are shown (A29 HN–F75 CO, L77 HN–S27 CO, and K78 HN–P25 CO). The right panel shows a front cartoon view with the hydrogen bond stabilizing loop 2 shown (L55 H^N–side-chain COO[−] group of D48). In both views, the backbone representations of residues with amide protons that have not exchanged with D₂O after 2 months are colored blue (V8, A9, I11, I12, and A13 of $\alpha1$, I47 of $\alpha2$, and L80, A81, R83, I84, D85, and L87 of $\alpha5$). (D) Structural comparison of holo-RpAcpXL (yellow) with *E. coli* heptanoyl-ACP (purple) (PDB entry 2FAD-A). (E) Worm representation of holo-RpAcpXL scaled by the weighted average chemical shift difference between ^1H and ^{15}N resonances⁵⁴ in apo- and holo-RpAcpXL, $\Delta\delta_{\text{av}}$, where $\Delta\delta_{\text{av}} = \{^{1/2}[(\Delta\delta\text{H}^{\text{N}})^2 + (\Delta\delta\text{N}/5)^2]\}^{1/2}$, $\Delta\delta\text{H}^{\text{N}} = \delta\text{H}^{\text{N}}_{\text{apo}} - \delta\text{H}^{\text{N}}_{\text{holo}}$, and $\Delta\delta\text{N} = \delta\text{N}_{\text{apo}} - \delta\text{N}_{\text{holo}}$. Side chains with chemical shift changes (≥ 0.05 for ^1H and ≥ 0.3 for ^{13}C) are shown: I35, S37, and L55 in loop 2 and Q73 and Y74 in $\alpha4$. Smaller chemical shift differences (≥ 0.04 for ^1H and ≥ 0.2 for ^{13}C) were observed for L57 and W60 in $\alpha4$ and F40 in $\alpha2$ across from L57. (F) Back and front views of the ConSurf³⁸ image (same orientation as panel C). Sixty KEGG orthologs were used in the alignment. Magenta denotes highly conserved residues and cyan variable. All structural figures in this paper were created with PyMol.

Information). Although only the first site is conserved, shifts for both D36 and D48 indicate weak binding at two sites with K_d values of 10–20 mM (Figure S3B,C of the Supporting Information). Weak Mg^{2+} binding can likely be attributed to the high concentration of monovalent cations in the NMR buffer, containing 200 mM NaCl. This was the case for *E. coli* ACP, where high concentrations of KCl or NaCl reduced the divalent cation binding affinities.^{33,34} It is likely that both types of cations can result in stabilization of the structure by neutralization of the acidic character of the protein. The weak Mg^{2+} binding and small spectral changes suggest that the structure of RpAcpXL was not significantly perturbed by binding.

An overlay of apo- and holo-RpAcpXL ^1H – ^{15}N HSQC spectra showed shifted resonances, with only S37 and L55 shifted by more than 0.1 ppm in the ^1H dimension (Figures S4 and S5 of the Supporting Information). The chemical shift differences between H^N resonances for apo- and holo-protein samples are plotted on the structure in Figure 1E. As expected, the largest chemical shift differences were for conserved resonances, D36, S37, and L38, a result previously reported for *E. coli* ACP.³⁶ These chemical shift changes were the result of covalent and transient interactions with the 4'-PP. Interestingly, the H^N resonances in loop 2, including L55,

also had chemical shift changes. This indicated that there were differences in this hinge region between the apo and holo conformations. This was further supported by side-chain ^1H and ^{13}C chemical shifts changes (≥ 0.05 for ^1H and ≥ 0.3 for ^{13}C) for residues within the hydrophobic cavity and $\alpha4$, in addition to those for I35 and S37 (Figure 1E). The chemical shift changes upon modification by 4'-PP may reflect small differences in the hydrophobic cavity environment that were not detected by the NOE-based structure determination.

Apo- and Holo-RpAcpXL Backbone ^{15}N Dynamics and Hydrogen–Deuterium (H–D) Exchange Experiments.

Despite the observed chemical shift differences between apo- and holo-RpAcpXL, no differences in backbone dynamics on the picosecond to nanosecond time scale were detected on the basis of analysis of two-dimensional ^{15}N T_1 , T_2 , and $^{15}\text{N}\{^1\text{H}\}$ heteronuclear NOE data (Figure 2). The average T_2 values were 85 ms, which is shorter than the T_2 of 100 ms expected for a monomer of this molecular weight. This could indicate slower overall backbone motions due to global conformational flexibility. However, the contribution of a small amount of oligomer could also cause this shorter T_2 and cannot be ruled out. The T_1/T_2 ratios for both apo- and holo-RpAcpXL (Figure 2) were also very similar with the exception of S37 that had the largest ratio (12.2 for apo and 16.4 for holo), indicating that

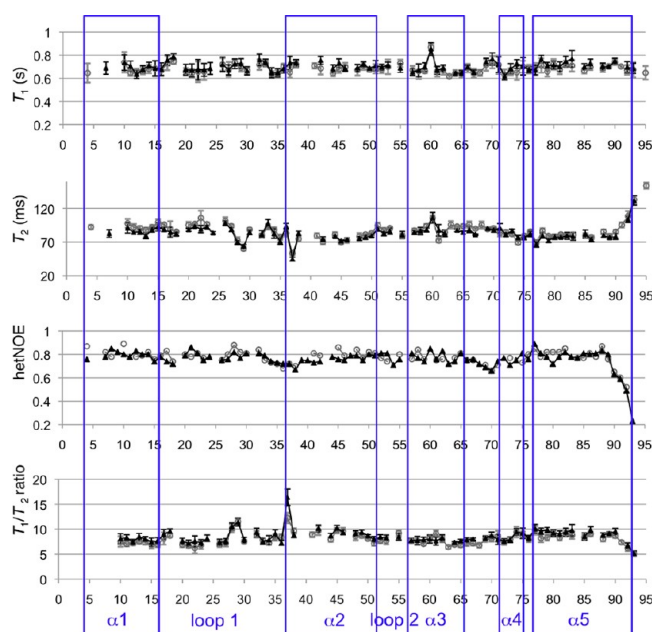


Figure 2. Summary of ^{15}N dynamics for apo- and holo-RpAcpXL. T_1 , T_2 , $^{15}\text{N}\{^1\text{H}\}$ heteronuclear NOE, and T_1/T_2 values are displayed as a function of amino acid residue. The data for apo-RpAcpXL are colored gray and the data for holo-RpAcpXL black.

microsecond to millisecond time scale motion contributed to relaxation for this residue. It is interesting that S37 showed slower time scale motion than the rest of the protein even in apo-RpAcpXL, a feature that could influence binding to AcpS. After modification by 4'-PP, the HN group of S37 exhibited even slower time scale motion with the largest change in the T_1/T_2 ratio between apo- and holo-RpAcpXL. This change in dynamics resulting from the 4'-PP modification could be an allosteric control mechanism for regulating interactions with other proteins.

Although the backbone ^{15}N dynamics data did not indicate that any of the helices had more flexibility on the picosecond to nanosecond time scale compared to the others, H^{N} H–D exchange data revealed that $\alpha 1$ and $\alpha 5$ had significantly slower amide proton exchange rates, on the order of days to weeks, than $\alpha 3$ and $\alpha 4$. In both apo- and holo-RpAcpXL, several residues in $\alpha 1$, $\alpha 2$, and $\alpha 5$ were still not exchanged by D_2O 2 months after lyophilization and resuspension into D_2O (Figure 1C and Figure S6 of the Supporting Information). These regions of slow H–D exchange indicated a stable core on the “backside” of this protein that experienced less local conformational dynamics associated with breaking of hydrogen bonds that allow amide proton exchange. The loops, $\alpha 3$ and $\alpha 4$, and the N-terminal half of $\alpha 2$ did not have any amides with slow H–D exchange, suggesting greater conformational flexibility.

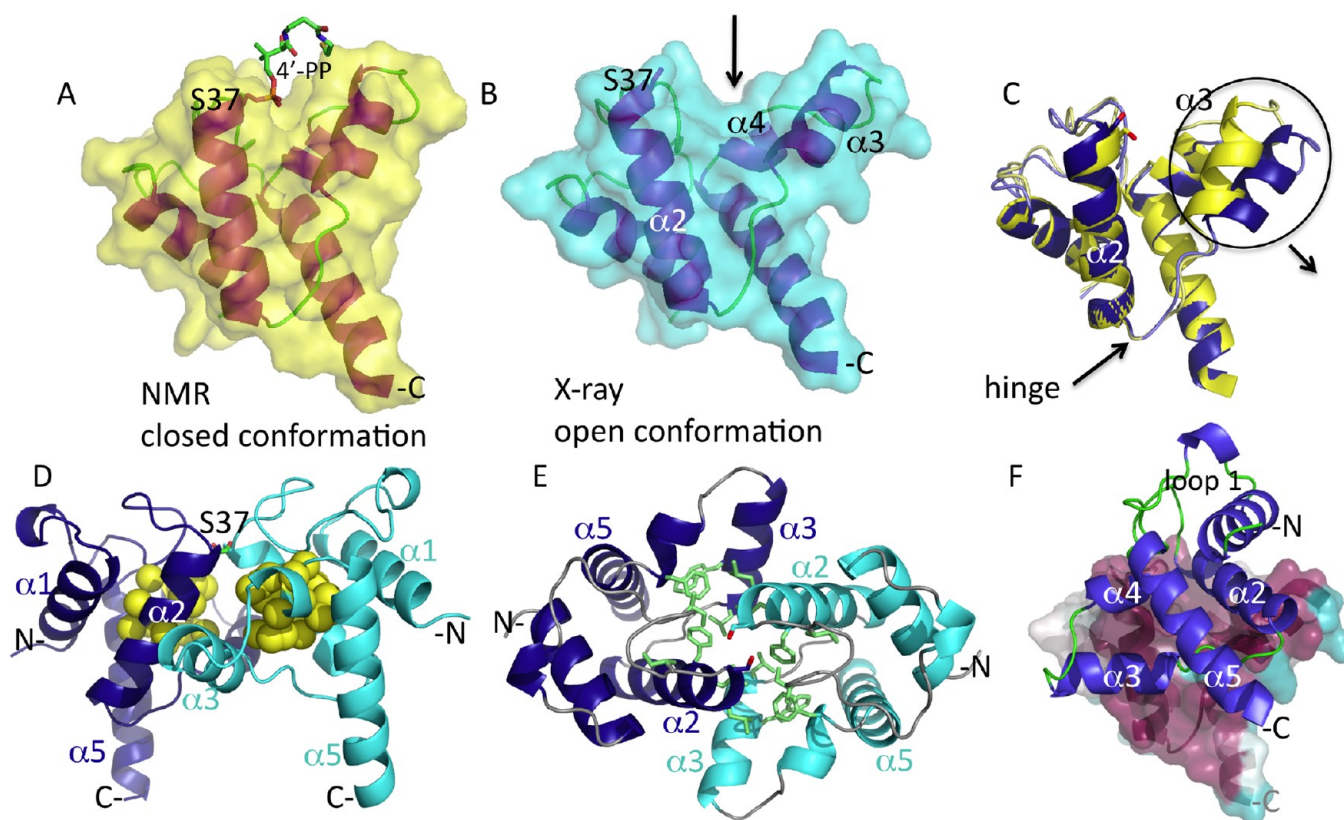


Figure 3. (A) Ribbon drawing with transparent surface representation of the holo-RpAcpXL NMR structure (PDB entry 2LL8) with a closed conformation. (B) Same representation for the apo-RpAcpXL crystal structure (PDB entry 3LMO) in the open conformation with the entrance to the hydrophobic cavity indicated by an arrow. (C) Structural comparison of holo-RpAcpXL NMR (yellow) and apo-RpAcpXL crystal (purple) structures indicating the difference conformation of $\alpha 3$. (D) Homodimer representation of the apo-RpAcpXL crystal structure with hydrophobic pocket predictions from CASTp²⁹ (residues A29, F40, I43, A44, I47, L55, L57, W60, Y74, F75, and L80; pockets 4 and 17, using a 1.4 Å probe radius to determine the solvent-accessible pocket volumes, vol_{ms}) indicated with yellow spheres. (E) Homodimer with hydrophobic side chains that are <5 Å from residues in the other subunit shown as sticks (I30, I35, L38, F40, L41, L57, W60, and F75). (F) ConSurf³⁸ image of the apo-RpAcpXL homodimer using the same sequences and colors as in Figure 1F.

These results are similar to those reported for *E. coli* ACP where residues in loop 1 and $\alpha 3$ exchanged the fastest.³⁷ All of the *E. coli* ACP amides exchanged in <1 day under the conditions studied.³⁷ The slower exchange rates for residues in RpAcpXL indicated that it was more stable to conformational unfolding than the *E. coli* ACP. In RpAcpXL, $\alpha 2$ and $\alpha 3$ on the “front” of the protein contain more conserved surface residues, based on ConSurf analysis³⁸ indicating that these residues are important for the function of proteins in this AcpXL family (Figure 1F). There were no differences in amide proton D₂O exchange rates between apo- and holo-RpAcpXL, indicating that the 4'-PP modification of S37 did not stabilize protein structure or alter the conformational dynamics in the vicinity of the modification as probed by H–D exchange.

Apo-RpAcpXL X-ray Structure. The X-ray structure of apo-RpAcpXL had an open conformation of the hydrophobic pocket compared to either the apo- or holo-NMR structures because of movement of $\alpha 3$ (Figure 3A–C). Structure and quality statistics for this crystal structure are listed in Table 3. Although RpAcpXL was primarily a monomer in solution at the high concentrations required for structure determination by NMR, with up to 13% dimer measured in solution by “GF/LS” experiments (data not shown), analysis of the molecular interface properties in the crystal structure by PDBePISA³⁹ indicated that the most likely biological assembly of RpAcpXL is a homodimer with $\sim 880 \text{ \AA}^2$ of buried protein surface (Figure 3D). In the predicted homodimer structure, $\alpha 2$ and $\alpha 3$ from each subunit pack together in a reciprocal manner, so the proteins are “front to front” and the S37 residues from each chain are close together (Figure 3D,E). According to CASTp calculations,²⁴ each subunit has a hydrophobic cavity in the center of the helical bundle with S37 at the entrance to the cavity with a volume of 120 \AA^3 (Figure 3D). These hydrophobic cavities are close together, and several hydrophobic residues in the cavity are <5 Å from residues in the other subunit (Figure 3E). The conserved surface residues are located at the dimer interface as visualized by ConSurf,³⁸ giving further evidence that this interface represents the biological assembly (Figure 3F). Biological interfaces are typically conserved and the largest contact in the crystal.⁴⁰ Using information about conserved residues was able to improve predictions of homodimer biological versus nonbiological interfaces to high accuracy.⁴⁰ It is possible that the biological significance of the homodimer, if it is the biologically active assembly, is to create a large shared hydrophobic cavity between the subunits that could accommodate a very long-chain fatty acid during synthesis and transfer to lipid A.

DISCUSSION

The structure of RpAcpXL is the first for the family of AcpXL proteins. According to the DOOR web resource (Database for prokaryotic Operons),⁴¹ the genomic context of RpAcpXL is the same as for *S. meliloti* and *R. leguminosarum* (Figure S7 of the Supporting Information). There are six genes with a two-operon transcriptional organization with the first operon encoding the AcpXL along with three other proteins involved in VLCFA synthesis and a second operon encoding two proteins, a putative alcohol dehydrogenase, AdhA2XL, and VLCFA acyl transferase, LpxXL. The LpxXL is believed to be responsible for transferring VLCFA from the AcpXL to lipid A.^{6,11,42} In fact, mutation of any of the genes in the *acpXL-lpxXL* gene cluster in *S. meliloti* resulted in the loss of VLCFA-LPS.³

To synthesize holo-RpAcpXL, *E. coli* AcpS was used via enzymatic conversion. The rapid conversion to completion was surprising because RpAcpXL shares only 32% sequence identity with the ACP from *E. coli*. However, proteins with even less sequence similarity were able to undergo the 4'-PP modification via enzymatic conversion by AcpS.¹⁵ RpAcpXL contains the conserved DSL sequence motif as well as acidic residues in $\alpha 2$, D42 and D48, that are important for recognition by the AcpS.⁴³

The structure of RpAcpXL has an extra helix compared to most other previously determined ACP structures. As a result, the opening to the hydrophobic cavity is larger. Upon modification by 4'-PP, there were no observable changes in structure or backbone dynamics on the picosecond to nanosecond time scale, although there were chemical shift perturbations. It is possible that subtle differences in chemical structure may be necessary to modulate interactions with enzymes involved in the synthesis and transfer of the VLCFA to lipid A, although it may be that addition of the 4'-PP is all that is needed to provide functionality to the AcpXL.

In addition, the apo-RpAcpXL crystal structure indicated that dimerization may be important for the biological activity of AcpXL. This hypothesis is based on the fact that (i) dimerization occurs in solution to some extent under various buffer conditions, (ii) the predicted dimerization interface has $>800 \text{ \AA}^2$ of buried protein surface and contains conserved surface residues, (iii) dimerization results in structural changes that create a large shared hydrophobic cavity, and (iv) RpAcpXL synthesizes a VLCFA that is twice as long as the well-studied *E. coli* ACP and therefore may require a hydrophobic cavity that is twice as large. However, because the biological relevance of dimerization has not been experimentally confirmed, it is possible that (i) it is an artifact of the high protein concentrations in solution, (ii) the predicted dimerization interface is a crystal packing artifact, and (iii) the structural rearrangement to the open conformation upon dimerization may reflect intrinsic changes in RpAcpXL that may occur in response to binding to other enzymes in the VLCFA pathway and may not be an allusion to the biological significance of dimerization. NMR-based estimations of τ_c and GF/LS screening of RpAcpXL with the Tris-HCl buffer (pH 7.5) used to set up the crystal trials indicate that the protein is monomeric under these conditions (data not shown). Interestingly, lowering the pH below 5 resulted in some precipitation (data not shown). This suggests that oligomerization may occur at lower pH values, such as those determined for crystallization, mixing the protein in the high-pH buffer with the 0.1 M sodium citrate buffer (pH 4.2).

The binding partners for AcpXL have not yet been characterized, with the exception of LpxXL, the long-chain acyltransferase. It is likely that AcpXL interacts with all the proteins produced by genes in the six-gene cluster responsible for the synthesis of VLCFA-modified lipid A.^{2–4} It also remains unknown whether AcpXL interacts with FA synthesis or other canonical LPS synthesis enzymes. The fatty acid chain could be transferred from the “standard” FA synthesis ACP to the AcpXL and then subsequently elongated with other enzymes found in the *acpXL-lpxXL* gene cluster to synthesize acyl-AcpXL with a VLCFA.

Structures of AcpXL in complex with the VLCFA enzymes and the possible biological relevance of AcpXL dimerization remain to be determined. However, if dimerization is biologically relevant, it might preclude certain enzymes from

binding to $\alpha 2$ in AcpXL. On the basis of the predicted dimer structure of RpAcpXL, binding proteins could still interact with both the N- and C-termini of $\alpha 2$. However, $\alpha 3$ in the other subunit is perpendicular to $\alpha 2$ and crosses in the middle of $\alpha 2$ (near F45). In *E. coli* ACP, $\alpha 2$ is crucially important for the binding with AcpS as well as enzymes involved in FA and LPS synthesis (reviewed in refs 44–46). AcpS and other ACP-binding proteins typically have a conserved positively charged Arg residue in a hydrophobic patch adjacent to their active site, which can form contacts with the hydrophobic and acidic residues in $\alpha 2$ of ACP (reviewed in refs 44 and 46). For FA synthesis ACPs, it has been determined that residues at the N-terminus of $\alpha 2$ (near S37) were important for binding to all partners, and residues near the C-terminus of $\alpha 2$ were also important for binding to some enzymes.^{44,47,48} For example, binding to LpxA, the acyltransferase that catalyzes the first step of lipid A biosynthesis, is affected by residues along the length of *Vibrio harveyi* ACP $\alpha 2$.^{48,49} It remains to be determined whether dimerization has an effect on binding of VLCFA synthesis proteins to AcpXL and if it is important for the function of the AcpXL family proteins.

■ ASSOCIATED CONTENT

■ Supporting Information

Figures, tables, and text containing supplementary methods, rotational correlation time estimation, mass spectrometry data, overlaid NMR ^1H – ^{15}N spectra, changes in ^1H and ^{15}N chemical shifts upon removal of Ca^{2+} , upon titration with MgCl_2 , and upon conversion to holo-RpAcpXL, ^{15}N dynamics, and *rpa2022* genomic context. This material is available free of charge via the Internet at <http://pubs.acs.org>.

■ AUTHOR INFORMATION

Corresponding Author

*T.A.R.: Department of Chemistry and Biochemistry, Miami University, Oxford, OH 45056; e-mail, ramelota@miamioh.edu; phone, (513) 593-2402; fax, (513) 529-5715. M.A.K.: Department of Chemistry and Biochemistry, Miami University, Oxford, OH 45056; e-mail, kennedm4@miamioh.edu; phone, (513) 529-8267; fax, (513) 529-5715.

Funding

This work was supported by grants from the National Institute of General Medical Sciences Protein Structure Initiative (PSI) of the National Institutes of Health, PSI-2 (P50 GM074958) and PSI:Biological (U54-GM094597).

Notes

The authors declare no competing financial interest.

■ ACKNOWLEDGMENTS

We thank Alexander Lemak for valuable scientific discussions and John A. Schwanof and Randy Abramowitz for their support at beamline X4 (National Synchrotron Light Source, Brookhaven National Laboratory, Upton, NY). The *E. coli* AcpS clone was kindly provided by Rosa Di Leo and Alexei Savchenko's group at the Ontario Centre for Structural Proteomics (affiliated with the Midwest Center for Structural Genomics). NMR data were collected at the Ohio Center of Excellence in Biomedicine in Structural Biology and Metabonomics at Miami University.

■ ABBREVIATIONS

ACP, acyl carrier protein; NMR, nuclear magnetic resonance; RDC, residual dipolar coupling; NOE, nuclear Overhauser effect; HSQC, heteronuclear single-quantum coherence spectroscopy; rmsd, root-mean-square deviation; FAS, fatty acid synthesis; LPS, lipopolysaccharide; 4'-PP, 4'-phosphopantetheine; CoA, coenzyme A; LPS OH-FA, lipopolysaccharide hydroxy fatty acids; VLCFA, very long-chain fatty acid.

■ REFERENCES

- (1) Brozek, K. A., Carlson, R. W., and Raetz, C. R. (1996) A special acyl carrier protein for transferring long hydroxylated fatty acids to lipid A in *Rhizobium*. *J. Biol. Chem.* 271, 32126–32136.
- (2) Vedam, V., Kannenberg, E., Datta, A., Brown, D., Haynes-Gann, J. G., Sherrier, D. J., and Carlson, R. W. (2006) The pea nodule environment restores the ability of a *Rhizobium leguminosarum* lipopolysaccharide *acpXL* mutant to add 27-hydroxyoctacosanoic acid to its lipid A. *J. Bacteriol.* 188, 2126–2133.
- (3) Haag, A. F., Wehmeier, S., Muszyński, A., Kerscher, B., Fletcher, V., Berry, S. H., Hold, G. L., Carlson, R. W., and Ferguson, G. P. (2011) Biochemical characterization of *Sinorhizobium meliloti* mutants reveals gene products involved in the biosynthesis of the unusual lipid A very long-chain fatty acid. *J. Biol. Chem.* 286, 17455–17466.
- (4) Brown, D. B., Huang, Y.-C., Kannenberg, E. L., Sherrier, D. J., and Carlson, R. W. (2011) An *acpXL* mutant of *Rhizobium leguminosarum* bv. phaseoli lacks 27-hydroxyoctacosanoic acid in its lipid A and is developmentally delayed during symbiotic infection of the determinate nodulating host plant *Phaseolus vulgaris*. *J. Bacteriol.* 193, 4766–4778.
- (5) Ramadas Bhat, U., Carlson, R. W., Busch, M., and Mayer, H. (1991) Distribution and phylogenetic significance of 27-hydroxyoctacosanoic acid in lipopolysaccharides from bacteria: Belonging to the α -2 subgroup of *proteobacteria*. *Int. J. Syst. Bacteriol.* 41, 213–217.
- (6) Sharypova, L. A., Niehaus, K., Scheidle, H., Holst, O., and Becker, A. (2003) *Sinorhizobium meliloti acpXL* mutant lacks the C28 hydroxylated fatty acid moiety of lipid A and does not express a slow migrating form of lipopolysaccharide. *J. Biol. Chem.* 278, 12946–12954.
- (7) Vedam, V., Kannenberg, E. L., Haynes, J. G., Sherrier, D. J., Datta, A., and Carlson, R. W. (2003) A *Rhizobium leguminosarum* AcpXL mutant produces lipopolysaccharide lacking 27-hydroxyoctacosanoic acid. *J. Bacteriol.* 185, 1841–1850.
- (8) Vedam, V., Haynes, J. G., Kannenberg, E. L., Carlson, R. W., and Sherrier, D. J. (2004) A *Rhizobium leguminosarum* lipopolysaccharide lipid-A mutant induces nitrogen-fixing nodules with delayed and defective bacteroid formation. *Mol. Plant-Microbe Interact.* 17, 283–291.
- (9) Haag, A. F., Wehmeier, S., Beck, S., Marlow, V. L., Fletcher, V., James, E. K., and Ferguson, G. P. (2009) The *Sinorhizobium meliloti* LpxXL and AcpXL proteins play important roles in bacteroid development within alfalfa. *J. Bacteriol.* 191, 4681–4686.
- (10) Haag, A. F., Myka, K. K., Arnold, M. F. F., Caro-Hernández, P., and Ferguson, G. P. (2010) Importance of lipopolysaccharide and cyclic β -1,2-glucans in *Brucella*-mammalian infections. *Int. J. Microbiol.* 2010, 1–12.
- (11) Ferguson, G. P., Datta, A., Carlson, R. W., and Walker, G. C. (2005) Importance of unusually modified lipid A in *Sinorhizobium* stress resistance and legume symbiosis. *Mol. Microbiol.* 56, 68–80.
- (12) Butland, G., Peregrin-Alvarez, J. M., Li, J., Yang, W., Yang, X., Canadien, V., Starostine, A., Richards, D., Beattie, B., Krogan, N., Davey, M., Parkinson, J., Greenblatt, J., and Emili, A. (2005) Interaction network containing conserved and essential protein complexes in *Escherichia coli*. *Nature* 433, 531–537.
- (13) Gabanyi, M. J., Adams, P. D., Arnold, K., Bordoli, L., Carter, L. G., Flippin-Andersen, J., Gifford, L., Haas, J., Kouranov, A., McLaughlin, W. A., Micallef, D. I., Minor, W., Shah, R., Schwede, T., Tao, Y.-P., Westbrook, J. D., Zimmerman, M., and Berman, H. M. (2011) The Structural Biology Knowledgebase: A portal to protein

structures, sequences, functions, and methods. *J. Struct. Funct. Genomics* 12, 45–54.

(14) Acton, T. B., Xiao, R., Anderson, S., Aramini, J., Buchwald, W. A., Ciccocanti, C., Conover, K., Everett, J., Hamilton, K., Huang, Y. J., Janjua, H., Kornhaber, G., Lau, J., Lee, D. Y., Liu, G., Maglaqui, M., Ma, L., Mao, L., Patel, D., Rossi, P., Sahdev, S., Shastry, R., Swapna, G. V. T., Tang, Y., Tong, S., Wang, D., Wang, H., Zhao, L., and Montelione, G. T. (2011) Preparation of protein samples for NMR structure, function, and small-molecule screening studies. *Methods Enzymol.* 493, 21–60.

(15) Ramelot, T. A., Smola, M. J., Lee, H.-W., Ciccocanti, C., Hamilton, K., Acton, T. B., Xiao, R., Everett, J. K., Prestegard, J. H., Montelione, G. T., and Kennedy, M. A. (2012) Solution structure of 4'-phosphopantetheine - GmACP3 from *Geobacter metallireducens*: A specialized acyl carrier protein with atypical structural features and a putative role in lipopolysaccharide biosynthesis. *Biochemistry* 51, 1442–1453.

(16) Rossi, P., Aramini, J. M., Xiao, R., Chen, C. X., Nwosu, C., Owens, L. A., Maglaqui, M., Nair, R., Fischer, M., Acton, T. B., Honig, B., Rost, B., and Montelione, G. T. (2009) Structural elucidation of the Cys-His-Glu-Asn proteolytic relay in the secreted CHAP domain enzyme from the human pathogen *Staphylococcus saprophyticus*. *Proteins* 74, 515–519.

(17) Tjandra, N., Grzesiek, S., and Bax, A. (1996) Magnetic field dependence of nitrogen-proton J splittings in ¹⁵N-enriched human ubiquitin resulting from relaxation interference and residual dipolar coupling. *J. Am. Chem. Soc.* 118, 6264–6272.

(18) Rückert, M., and Otting, G. (2000) Alignment of biological macromolecules in novel nonionic liquid crystalline media for NMR experiments. *J. Am. Chem. Soc.* 122, 7793–7797.

(19) Hansen, M. R., Mueller, L., and Pardi, A. (1998) Tunable alignment of macromolecules by filamentous phage yields dipolar coupling interactions. *Nat. Struct. Mol. Biol.* 5, 1065–1074.

(20) Delaglio, F., Grzesiek, S., Vuister, G., Zhu, G., Pfeifer, J., and Bax, A. (1995) NMRPipe: A multidimensional spectral processing system based on UNIX pipes. *J. Biomol. NMR* 6, 277–293.

(21) Güntert, P. (2004) Automated NMR structure calculation with CYANA. *Methods Mol. Biol.* 278, 353–378.

(22) Shen, Y., Delaglio, F., Cornilescu, G., and Bax, A. (2009) TALOS+: A hybrid method for predicting protein backbone torsion angles from NMR chemical shifts. *J. Biomol. NMR* 44, 213–223.

(23) Brunger, A. T., Adams, P. D., Clore, G. M., DeLano, W. L., Gros, P., Grosse-Kunstleve, R. W., Jiang, J. S., Kuszewski, J., Nilges, M., Pannu, N. S., Read, R. J., Rice, L. M., Simonson, T., and Warren, G. L. (1998) Crystallography & NMR system: A new software suite for macromolecular structure determination. *Acta Crystallogr.* D54, 905–921.

(24) Linge, J. P., Williams, M. A., Spronk, C. A., Bonvin, A. M., and Nilges, M. (2003) Refinement of protein structures in explicit solvent. *Proteins* 50, 496–506.

(25) Lemak, A., Gutmanas, A., Chitayat, S., Karra, M., Farès, C., Sunnerhagen, M., and Arrowsmith, C. H. (2011) A novel strategy for NMR resonance assignment and protein structure determination. *J. Biomol. NMR* 49, 27–38.

(26) Otwinowski, Z., and Minor, W. (1997) Processing of X-ray diffraction data collected in oscillation mode. *Methods Enzymol.* 276, 307–326.

(27) Vagin, A., and Teplyakov, A. (1997) MOLREP: An automated program for molecular replacement. *J. Appl. Crystallogr.* 30, 1022–1025.

(28) Duncan, E. M. (1999) XtalView/Xfit: A versatile program for manipulating atomic coordinates and electron density. *J. Struct. Biol.* 125, 156–165.

(29) Dundas, J., Ouyang, Z., Tseng, J., Binkowski, A., Turpaz, Y., and Liang, J. (2006) CASTp: Computed atlas of surface topography of proteins with structural and topographical mapping of functionally annotated residues. *Nucleic Acids Res.* 34, W116–W118.

(30) Li, Q., Khosla, C., Puglisi, J. D., and Liu, C. W. (2003) Solution structure and backbone dynamics of the holo form of the frenolicin acyl carrier protein. *Biochemistry* 42, 4648–4657.

(31) Sharma, A. K., Sharma, S. K., Suroliya, A., Suroliya, N., and Sarma, S. P. (2006) Solution structures of conformationally equilibrium forms of holo-acyl carrier protein (PfACP) from *Plasmodium falciparum* provides insight into the mechanism of activation of ACPs. *Biochemistry* 45, 6904–6916.

(32) Evans, S. E., Williams, C., Arthur, C. J., Burston, S. G., Simpson, T. J., Crosby, J., and Crump, M. P. (2008) An ACP structural switch: Conformational differences between the apo and holo forms of the actinorhodin polyketide synthase acyl carrier protein. *ChemBioChem* 9, 2424–2432.

(33) Schulz, H. (1975) On the structure-function relationship of acyl carrier protein of *Escherichia coli*. *J. Biol. Chem.* 250, 2299–2304.

(34) Tener, D. M., and Mayo, K. H. (1990) Divalent cation binding to reduced and octanoyl acyl-carrier protein. *Eur. J. Biochem.* 189, 559–565.

(35) Frederick, A. F., Kay, L. E., and Prestegard, J. H. (1988) Location of divalent ion sites in acyl carrier protein using relaxation perturbed 2D NMR. *FEBS Lett.* 238, 43–48.

(36) Kim, Y., Kovrigin, E. L., and Eletr, Z. (2006) NMR studies of *Escherichia coli* acyl carrier protein: Dynamic and structural differences of the apo- and holo-forms. *Biochem. Biophys. Res. Commun.* 341, 776–783.

(37) Andrec, M., Blake Hill, R., and Prestegard, J. H. (1995) Amide exchange rates in *Escherichia coli* acyl carrier protein: Correlation with protein structure and dynamics. *Protein Sci.* 4, 983–993.

(38) Ashkenazy, H., Erez, E., Martz, E., Pupko, T., and Ben-Tal, N. (2010) ConSurf 2010: Calculating evolutionary conservation in sequence and structure of proteins and nucleic acids. *Nucleic Acids Res.* 38, W529–W533.

(39) Krissinel, E., and Henrick, K. (2007) Inference of macromolecular assemblies from crystalline state. *J. Mol. Biol.* 372, 774–797.

(40) Valdar, W. S. J., and Thornton, J. M. (2001) Conservation helps to identify biologically relevant crystal contacts. *J. Mol. Biol.* 313, 399–416.

(41) Mao, F., Dam, P., Chou, J., Olman, V., and Xu, Y. (2009) DOOR: A database for prokaryotic operons. *Nucleic Acids Res.* 37, D459–D463.

(42) Basu, S. S., Karbarz, M. J., and Raetz, C. R. (2002) Expression cloning and characterization of the C28 acyltransferase of lipid A biosynthesis in *Rhizobium leguminosarum*. *J. Biol. Chem.* 277, 28959–28971.

(43) Parris, K. D., Lin, L., Tam, A., Mathew, R., Hixon, J., Stahl, M., Fritz, C. C., Seehra, J., and Somers, W. S. (2000) Crystal structures of substrate binding to *Bacillus subtilis* holo-(acyl carrier protein) synthase reveal a novel trimeric arrangement of molecules resulting in three active sites. *Structure* 8, 883–895.

(44) Zhang, Y. M., Rao, M. S., Heath, R. J., Price, A. C., Olson, A. J., Rock, C. O., and White, S. W. (2001) Identification and analysis of the acyl carrier protein (ACP) docking site on β -ketoacyl-ACP synthase III. *J. Biol. Chem.* 276, 8231–8238.

(45) Zhang, Y. M., Marrakchi, H., White, S. W., and Rock, C. O. (2003) The application of computational methods to explore the diversity and structure of bacterial fatty acid synthase. *J. Lipid Res.* 44, 1–10.

(46) Chan, D. I., and Vogel, H. J. (2010) Current understanding of fatty acid biosynthesis and the acyl carrier protein. *Biochem. J.* 430, 1–19.

(47) Rafi, S., Novichenok, P., Kolappan, S., Zhang, X., Stratton, C. F., Rawat, R., Kisker, C., Simmerling, C., and Tonge, P. J. (2006) Structure of acyl carrier protein bound to FabI, the FASII enoyl reductase from *Escherichia coli*. *J. Biol. Chem.* 281, 39285–39293.

(48) Gong, H., Murphy, A., McMaster, C. R., and Byers, D. M. (2007) Neutralization of acidic residues in helix II stabilizes the folded conformation of acyl carrier protein and variably alters its function with different enzymes. *J. Biol. Chem.* 282, 4494–4503.

- (49) Jain, N. U., Wyckoff, T. J. O., Raetz, C. R. H., and Prestegard, J. H. (2004) Rapid analysis of large protein–protein complexes using NMR-derived orientational constraints: The 95 kDa complex of LpxA with acyl carrier protein. *J. Mol. Biol.* 343, 1379–1389.
- (50) Moseley, H. N., Sahota, G., and Montelione, G. T. (2004) Assignment validation software suite for the evaluation and presentation of protein resonance assignment data. *J. Biomol. NMR* 28, 341–355.
- (51) Bhattacharya, A., Tejero, R., and Montelione, G. (2007) Evaluating protein structures determined by structural genomics consortia. *Proteins* 66, 778–795.
- (52) Zweckstetter, M. (2008) NMR: Prediction of molecular alignment from structure using the PALES software. *Nat. Protoc.* 3, 679–690.
- (53) Huang, Y. J., Powers, R., and Montelione, G. T. (2005) Protein NMR recall, precision, and F-measure scores (RPF scores): Structure quality assessment measures based on information retrieval statistics. *J. Am. Chem. Soc.* 127, 1665–1674.
- (54) Grzesiek, S., Bax, A., Clore, G. M., Gronenborn, A. M., Hu, J.-S., Kaufman, J., Palmer, I., Stahl, S. J., and Wingfield, P. T. (1996) The solution structure of HIV-1 Nef reveals an unexpected fold and permits delineation of the binding surface for the SH3 domain of Hck tyrosine protein kinase. *Nat. Struct. Biol.* 3, 340–345.